

Unbiased mm-wave Line Surveys of TW Hya and V4046 Sgr: The Enhanced C₂H and CN Abundances of Evolved Protoplanetary Disks

Joel H. Kastner¹, Pierre Hily-Blant², David R. Rodriguez³, Kristina Punzi¹, Thierry Forveille²

ABSTRACT

We have conducted the first comprehensive mm-wave molecular emission line surveys of the evolved circumstellar disks orbiting the nearby, roughly solar-mass, pre-main sequence (T Tauri) stars TW Hya ($D = 54$ pc) and V4046 Sgr AB ($D = 73$ pc). Both disks are known to retain significant residual gaseous components, despite the advanced ages of their host stars (~ 8 Myr and ~ 21 Myr, respectively). Our unbiased broad-band radio spectral surveys of the TW Hya and V4046 Sgr disks were performed with the Atacama Pathfinder Experiment (APEX) 12 meter telescope and are intended to yield a complete census of bright molecular emission lines in the range 275–357 GHz (1.1–0.85 mm). We find that lines of ¹²CO, ¹³CO, HCN, CN, and C₂H, all of which lie in the higher-frequency (>330 GHz) range, constitute the strongest molecular emission from both disks in the spectral region surveyed. The molecule C₂H is detected here for the first time in both disks, as is CS in the TW Hya disk. The survey results also include the first measurements of the full suite of hyperfine transitions of CN $N = 3 \rightarrow 2$ and C₂H $N = 4 \rightarrow 3$ in both disks. Modeling of these CN and C₂H hyperfine complexes in the spectrum of TW Hya indicates that the emission from both species is optically thick and may originate from very cold ($\lesssim 10$ K) disk regions. The latter result, if confirmed, would suggest efficient production of CN and C₂H in the outer disk and/or near the disk midplane. It furthermore appears that the fractional abundances of CN and C₂H are significantly enhanced in these evolved protoplanetary disks relative to the fractional abundances of the same molecules in the environments of deeply

¹Center for Imaging Science, School of Physics & Astronomy, and Laboratory for Multiwavelength Astrophysics, Rochester Institute of Technology, 54 Lomb Memorial Drive, Rochester NY 14623 USA (jhk@cis.rit.edu)

²UJF-Grenoble 1/CNRS-INSU, Institut de Planétologie et d'Astrophysique de Grenoble (IPAG) UMR 5274, 38041, Grenoble, France

³Departamento de Astronomía, Universidad de Chile, Casilla 36-D, Santiago, Chile

embedded protostars. These results, combined with previous determinations of enhanced abundances of other species (such as HCO^+) in T Tauri star disks, underscore the importance of properly accounting for high-energy (FUV and X-ray) radiation from the central T Tauri star when modeling protoplanetary disk gas chemistry and physical conditions.

1. Introduction

Millimeter and submm interferometric studies of molecular emission from the nearest and most evolved known examples of dusty disks orbiting pre-main sequence (pre-MS) stars provide a unique means to ascertain the physical conditions and chemistry within outer ($R > 10$ AU) disk regions (see reviews in Williams & Cieza 2011; Dutrey et al. 2014). In evolved disks with ages of a few Myr, these regions are likely undergoing the buildup and orbital migration of giant planets and icy planetesimals (e.g., Hubbard et al. 2002; Luu & Jewitt 2002). Submillimeter molecular line observations thereby serve to clarify the “voyage” of organic material from interstellar clouds to gaseous and icy outer solar system bodies (Ehrenfreund & Charnley 2000).

Theorists have increasingly focused on pre-MS star UV and X-ray radiation as potential drivers of the processing of planet-forming gas and dust in disks, via the profound effects of such radiation on disk gas heating and chemistry (e.g., Glassgold et al. 1997, 2004, 2009, 2012; Stäuber et al. 2005; Gorti & Hollenbach 2008; Meijerink et al. 2008; Ercolano et al. 2008, 2009; Drake et al. 2009; Gorti et al. 2009, 2011; Owen et al. 2010, 2011; Walsh et al. 2012; Aresu et al. 2012; Cleeves et al. 2013). In parallel, we and others are undertaking submillimeter observations of potential molecular tracers of disk irradiation, so as to inform and test such models (e.g., Kastner et al. 2008; Qi et al. 2008; Henning et al. 2010; Salter et al. 2011; Öberg et al. 2011; Chapillon et al. 2012).

At distances of only 54 and 73 pc, respectively (Torres et al. 2008, and refs. therein), the relatively old (age ~ 10 Myr) yet still actively accreting pre-MS star/disk systems TW Hya and V4046 Sgr offer unparalleled opportunities to study late-stage disk dissipation and planet-building processes at close range. Given their roughly solar-mass central stars, these circumstellar environments are likely similar to that of the early solar system — with the important and intriguing caveat that TW Hya is a single star of mass $\sim 0.8 M_\odot$ (Andrews et al. 2012), whereas V4046 Sgr is a close ($P \sim 2.4$ day) binary system consisting of nearly equal-mass, $\sim 0.9 M_\odot$ components (Rosenfeld et al. 2012a). Despite their advanced ages (estimated as ~ 8 Myr and ~ 21 Myr, respectively; Torres et al. 2008; Binks & Jeffries 2014; Ducourant et al. 2014), the circumstellar disks orbiting TW Hya and V4046 Sgr both retain

substantial reservoirs of molecular gas — according to some estimates, as much as $\sim 0.05\text{--}0.1 M_{\odot}$ of H_2 — as evidenced by relatively strong emission lines of CO and other trace molecular species detected and mapped thus far (e.g., Kastner et al. 1997, 2008; Thi et al. 2004; Qi et al. 2004, 2006, 2008; Rodriguez et al. 2010; Öberg et al. 2011; Andrews et al. 2012; Rosenfeld et al. 2012b,a, 2013; Bergin et al. 2013). These results have established the importance of the disks orbiting TW Hya and V4046 Sgr to studies of disk molecular chemistry and disk dissipation processes (for a summary of the properties of these two star/disk systems, see Table 3 in Sacco et al. 2014). In particular, submm molecular line observations of these two disks suggest that the abundances of certain species — such as HCN, CN, and HCO^+ , all of which are well-detected in these and other, similarly evolved disks orbiting active, late-type stars — are enhanced by strong UV and X-ray irradiation from chromospheres, coronae, and accretion shocks associated with the central stars (Kastner et al. 1997, 2008; Thi et al. 2004).

Unbiased single-dish radio molecular spectral line surveys have long been recognized as a powerful means to efficiently assess the molecular inventory of star-forming regions (e.g., Johansson et al. 1984; Blake et al. 1986, 1994; van Dishoeck et al. 1995; Schilke et al. 1997; Kaifu et al. 2004; Caux et al. 2011; Watanabe et al. 2012, and references therein). In the era of the Atacama Large Millimeter Array (ALMA), such surveys loom even more important, given the need to direct high-resolution ALMA interferometric imaging studies to the brightest and/or most physically and chemically interesting molecular species. Until very recently, it would have been impractical to perform an unbiased single-dish line survey of a molecular disk, due to the general weakness of disk emission lines (a consequence of the small beam filling factors of a typical disk). With the increasing sensitivity and bandwidth of radio receivers and spectrometers, however, it is now possible to carry out such surveys — at least for those gaseous disks that are nearest to Earth and, hence, largest in angular diameter.

The nearby, chemically rich molecular disks orbiting TW Hya and V4046 represent two obvious subjects for such “blind” line surveys in the (sub)mm regime. To investigate gas physical conditions and chemistry in these two disks, and to assess the impact of stellar irradiation more specifically, we have used the 12 m Atacama Pathfinder EXperiment (APEX¹) telescope to perform line surveys of TW Hya and V4046 Sgr over the 0.85–1.1 mm wavelength range.

¹<http://www.apex-telescope.org/>

2. Observations and Data Reduction

The line surveys of TW Hya and V4046 Sgr reported here were carried out with the APEX 12 m telescope and APEX-2 receiver in 2011 December and 2012 June (TW Hya) and 2012 April and May (V4046 Sgr). The precipitable water vapor fell in the range 0.2–0.4 mm during the observations. The Fast Fourier Transform Spectrometers (XFFTS2; Klein et al. 2006) were used as backends, providing 4 GHz instantaneous bandwidth coverage at 77 kHz (≈ 0.08 km s⁻¹) spectral resolution. The TW Hya and V4046 Sgr spectral surveys were conducted as sequences of 22 and 18 tuning setups, respectively, covering the 275 to 357 GHz frequency range (Fig. 1); the different sequences were the result of minor revisions to the observing scripts used to obtain the V4046 Sgr data. We avoided the 321 to 325 GHz interval where the atmosphere is strongly opaque. For each tuning, both polarizations were observed simultaneously, and integration proceeded until an rms channel-to-channel noise level of ≤ 20 mK was achieved in 0.5 km s⁻¹ spectral bins. For TW Hya, observations in most tuning setups were performed twice, with a 500 MHz frequency shift between the two, before shifting the central frequency upwards by 3 GHz. Fig. 2 summarizes fundamental observing and instrumental conditions (i.e., receiver and system temperatures and opacities) during the spectral surveys. The approximate total on-source observing times were ~ 1000 minutes and ~ 310 minutes for TW Hya and V4046 Sgr, respectively; the significantly shorter time spent observing the latter source reflects the superior conditions during those observations (Fig. 2).

Data reduction was performed with the CLASS software (Pety 2005). Reduction consisted of the standard steps, namely residual bandpass subtraction using polynomials and scan averaging with rms weighting. Baseline subtraction was mostly straightforward, thanks to the stability of the APEX instrumentation. Still, some so-called “platforming” effects were apparent; in such cases, the spectrum was split into a number of “platforms” from which low-order polynomials were subtracted individually. In other cases, baseline oscillations were present; these required higher-order (typically order 10) polynomial fitting, for removal. However, even such high-order fits are rather robust, given the very large number of channels (wide bandwidth) available. The averaging and stitching used a new, powerful scheme developed for CLASS spectral line data reduction², in which each spectrum is resampled onto a common spectral axis “on the fly”, only when needed.

The output of the foregoing data acquisition and reduction sequences for each of the two disk sources is a single spectrum that covers the full 275–357 GHz frequency range. The results for line intensities and derived quantities described in §3 were obtained from

²See <http://www.iram-institute.org/medias/uploads/class-average.pdf>

these spectra, adopting an antenna temperature to flux conversion (efficiency) of 41 Jy K^{-1} (corresponding to an aperture efficiency of 0.60 and a main-beam efficiency of 0.73) and a beam FWHM of $20''$; these represent mean values for APEX in the 0.8 mm window³.

3. Results and Analysis

3.1. Molecular line detections

Using spectral line identification methods available in the WEEDS extension of the GILDAS⁴ software tools combined with visual inspection, we have compiled lists of molecular transitions that are readily detectable and measurable in the 275–357 GHz APEX spectra of TW Hya and V4046 Sgr. A summary list of these molecular transitions is presented in Table 1. Spectral regions covering all lines detected from one or both disks are displayed in Fig. 3. This Figure illustrates how faint lines are more readily detectable in the APEX spectrum of TW Hya, despite the generally larger integrated line intensities measured for V4046 Sgr (Table 1), thanks to the relatively narrow linewidth of TW Hya (a consequence of this disk’s nearly face-on orientation; §3.2). Nevertheless, Fig 3 also makes clear the overall resemblance of the molecular spectra of TW Hya and V4046 Sgr in the 275–357 GHz band. Specifically, the strongest emission lines from both disks are confined to the higher-frequency (i.e., 330–355 GHz) spectral regions. The bright lines in this region include those of C_2H , which is detected here for first time in both the TW Hya and V4046 Sgr disks, as well as lines of species previously detected in both disks, i.e., CO, CN, and HCN (Kastner et al. 1997, 2008). The CN(3–2) and $\text{C}_2\text{H}(4-3)$ emission line strengths from both disks are exceeded only by that of ^{12}CO in this frequency range (Table 1; determinations of emission line intensities are described in §3.2). In addition, CS is detected for the first time in the TW Hya disk, in the form of emission from both the $J = 6 \rightarrow 5$ and $J = 7 \rightarrow 6$ rotational transitions.

Listings of all molecular transitions previously detected from the TW Hya and V4046 Sgr disks in the 215–365 GHz region, along with key transitions covered in the APEX line surveys reported here, are presented in Table 2. Molecular transitions measured and/or detected for the first time in our survey data are indicated in this Table. As these are the first 0.8–1.1 mm region spectral data obtained for V4046 Sgr, all lines seen in the APEX data for this disk constitute new detections. Furthermore, thanks to the broad spectral range of these line surveys, the APEX data for TW Hya and V4046 Sgr include complete coverage of

³See <http://www.apex-telescope.org/instruments/>.

⁴<http://www.iram.fr/IRAMFR/GILDAS/>

all hyperfine transitions of CN and C₂H within a specific rotational transition ($N = 3 \rightarrow 2$ and $N = 4 \rightarrow 3$, respectively; see §3.4).

3.2. Line intensity measurements

3.2.1. TW Hya

For the TW Hya disk — whose emission lines are quite narrow, due to its nearly pole-on viewing angle ($i \approx 7^\circ$; Qi et al. 2004) — line intensities, LSR velocities, and widths were measured using fitting tools available in CLASS, adopting a Gaussian line profile. The resulting intensities are listed (in units of Jy km s^{−1}) in Tables 1 and 2. Best-fit line LSR velocities and widths (which are not listed in these tables) lie in the range 2.84–2.96 km s^{−1} and 0.49–0.72 km s^{−1}, respectively, for all line detections with the exceptions of C¹⁸O(3–2) and H¹³CO⁺(4–3), for which the detections are marginal (Fig 3) and, hence, the best-fit line parameters are poorly determined. Given the typical fit uncertainties (0.05–0.1 km s^{−1}), these line-center velocities and velocity widths are consistent with each other and with those of molecular emission lines previously measured for TW Hya (e.g., Kastner et al. 1997; Thi et al. 2004). Discrepancies between our line intensity measurements and those obtained previously are evident in a few cases (e.g., for ¹²CO and HCN). Such discrepancies — which have been noted previously for certain TW Hya disk lines (e.g., Thi et al. 2004) — are most likely due to differences in beam sizes (we have not corrected for beam filling, in converting from K km s^{−1} to Jy km s^{−1}) as well as calibration uncertainties, which may be as large as ~40% for the weaker lines (Thi et al. 2004). In the case of CN and C₂H, we extended the line intensity modeling procedure to include a self-consistent treatment of hyperfine structure components (§3.4). Upper limits for nondetected transitions listed in Table 2 are 3σ and were obtained assuming a linewidth of 0.7 km s^{−1}.

3.2.2. V4046 Sgr

The V4046 Sgr disk is viewed at intermediate inclination ($i \approx 33^\circ$; Rodriguez et al. 2010; Rosenfeld et al. 2012a); as a result, its molecular line profiles are double-peaked. Hence, to determine the intensities of lines detected in our APEX survey (Tables 1), we adopt the approach of Kastner et al. (2008) to fit its line profiles. This method consists of fitting (via custom IDL codes) a parametric Keplerian line profile to determine the peak line intensity, outer disk radial velocity (v_d , equivalent to half of the peak-to-peak velocity width), the disk radial temperature profile power-law exponent (q), and outer disk density cutoff (p_d). Upon

obtaining a good fit, one can then integrate under the model line profile to obtain the total line intensity (I).

To determine v_d , we fit this parametric model to the $^{12}\text{CO}(3-2)$ line, fixing $q = 0.75$ and $p_d = 0.25$ (based on fits to lower J transitions of CO measured from the V4046 Sgr disk; Kastner et al. 2008). We find a peak line intensity of 13.3 ± 0.4 Jy and $v_d = 1.3 \pm 0.2$ km s $^{-1}$. The latter result is identical, to within the uncertainties, with the value determined for the $^{12}\text{CO}(2-1)$ line (Kastner et al. 2008). This best-fit model is overlaid on the observed $^{12}\text{CO}(3-2)$ line profile in Fig. 4. Although the reduced χ^2 is 1.1 for this fit, the model fails to reproduce the (shallow) dip between the peaks in the ^{12}CO line profile, and underestimates the emission in the profile’s (broad) red wing. These deficiencies are likely the result of the oversimplifications inherent in the parametric Keplerian model profile. As our purpose here is to obtain line intensity measurements (as opposed to physical inferences as to disk structure), however, the results described in subsequent sections are unaffected. To obtain intensity measurements of the other (much noisier) lines, including $^{13}\text{CO}(3-2)$, we fixed the model parameters to the foregoing values of v_d , q , and p_d , such that the only free parameter of the fits was the peak line intensity. The resulting fits to the $^{13}\text{CO}(3-2)$ and HCN(4–3) line profiles — two species that, like ^{12}CO , were previously detected in the V4046 Sgr disk — are also shown in Fig. 4. The best-fit peak line intensities for $^{13}\text{CO}(3-2)$ and HCN(4–3) are 4.0 ± 0.3 Jy and 3.0 ± 0.2 Jy, respectively, with reduced χ^2 values of 1.1 and 0.8. Upper limits for nondetected transitions listed in Tables 1 and 2 are 3σ and were obtained assuming the same value of v_d as found for $^{12}\text{CO}(3-2)$, i.e., $v_d = 1.3$ km s $^{-1}$.

3.3. Pure rotational transitions: column density estimates

We have used the results for integrated line intensities for the (pure rotational) transitions of ^{13}CO , HCN, and CS listed in Table 1 (as well as the molecular line reference data listed in that Table) to estimate source-averaged column densities for these molecules, using the methods described in Goldsmith & Langer (1999). Briefly, this involves calculating the upper level column density N_J for the transition $J \rightarrow (J - 1)$ via

$$N_J = \frac{8\pi k\nu^2 W}{hc^3 A_{J,J-1}} \left(\frac{\tau}{1 - e^{-\tau}} \right) f_{\text{dilution}}, \quad (1)$$

where ν is the frequency of the transition, W is the integrated line intensity (in K cm s $^{-1}$), τ is the optical depth in the transition, $f_{\text{dilution}} = \frac{\Omega_{mb} + \Omega_s}{\Omega_s}$ is the main-beam dilution correction factor (with Ω_{mb} and Ω_s the main-beam and source solid angles, respectively), and $A_{J,J-1}$ is

the Einstein coefficient for the transition, given by

$$A_{J,J-1} = \frac{64\pi^4\nu^3\mu^2}{3hc^3} \frac{J}{2J+1}, \quad (2)$$

with μ the permanent electric dipole moment of the molecule. The upper level column density can then be converted to total column density for a given molecular species via

$$N = N_J \frac{Q(T_{ex})}{g_J} e^{E_J/kT_{ex}}, \quad (3)$$

where the temperature-dependent rotational partition function is obtained from

$$Q(T_{ex}) \approx \frac{1}{3} + \frac{kT_{ex}}{hB_{rot}}, \quad (4)$$

with B_{rot} the molecular rotational constant. Eq. 4 is appropriate for linear (and approximately linear) molecules, i.e., for molecules with only one (or only one dominant) moment of inertia.

We used the foregoing methods to obtain source-averaged column densities N for a range of T_{ex} of 5–37.5 K. The upper end of this T_{ex} range is perhaps $\sim 30\%$ larger than the CO line excitation temperatures previously estimated for both disks (e.g., Qi et al. 2004; Rosenfeld et al. 2013), while the lower end roughly corresponds to the excitation temperature of C_2H as deduced from our analysis of C_2H hyperfine structure emission from TW Hya (§3.4). We assume optically thin emission, and adopt identical beam dilution factors of $f_{\text{dilution}} = 0.25$ for both disks and for all molecules in each disk. The latter is obtained by assuming that the characteristic emitting region radii R for all five molecules are the same as that of ^{12}CO , i.e., $R \approx 5''$ for both TW Hya and V4046 Sgr (Rosenfeld et al. 2012b, 2013). Since less abundant molecules likely have smaller effective beam filling factors than ^{12}CO (see, e.g., Fig. 6 in Rosenfeld et al. 2013), the source-averaged column densities of these species may be somewhat underestimated.

Results for N for ^{13}CO , HCN, and CS are listed in Table 3. The ^{13}CO column density we find for the TW Hya disk for the upper range of T_{ex} , $N(^{13}\text{CO}) \sim 2 \times 10^{14} \text{ cm}^{-2}$, is a factor ~ 2.5 smaller than the ^{13}CO column density previously determined by Thi et al. (2004) under the assumption $T_{ex} = 25 \text{ K}$. This difference in $N(^{13}\text{CO})$ values is mostly accounted for by the difference in assumed source radii (Thi et al. 2004, adopted a source radius of $\sim 3''$). The (disk-averaged) ^{13}CO column density we obtain for TW Hya assuming $T_{ex} = 18.75 \text{ K}$ and a beam filling factor $f_{\text{dilution}} = 0.25$ is furthermore consistent with the radially-dependent $N(^{13}\text{CO})$ values at large ($R \sim 100 \text{ AU}$) disk radii determined by Qi et al. (2013b) from fits of a detailed disk model to interferometric ^{13}CO data. Our HCN column density in this same T_{ex} range, $N(\text{HCN}) \sim 5 \times 10^{11} \text{ cm}^{-2}$, is more than an order of magnitude smaller than the

value of $N(\text{HCN})$ reported by Thi et al. (2004). This discrepancy is evidently due to their assuming optically thick HCN emission, in addition to a smaller source radius.

The estimated ^{13}CO column densities for V4046 Sgr are somewhat larger than those estimated for TW Hya (Table 3). This result — combined with the fact that the V4046 Sgr disk is also almost a factor 2 larger than that of TW Hya in linear radius — is consistent with various other indications that the V4046 Sgr molecular disk is more massive than that of TW Hya (Kastner et al. 2008; Rosenfeld et al. 2013; Bergin et al. 2013), despite the (factor ~ 2) greater age of the former system.

3.4. CN and C_2H hyperfine component analysis: optical depths, excitation temperatures, and column densities

3.4.1. TW Hya

The rotational state energy levels of the molecules CN and C_2H exhibit fine structure and hyperfine structure splitting (HFS) due to interactions between molecular rotational angular momentum with the electron and nuclear spins; these interactions result in a sequence of closely-spaced lines for each rotational state transition in the mm and submm (Table 4; see also, e.g., Ziurys et al. 1982). We performed measurement and analysis of the TW Hya CN $N = 3 \rightarrow 2$ and C_2H $N = 4 \rightarrow 3$ spectra — each of which is displayed, in its entirety, in Fig. 5 — using the classical HFS fitting method implemented in the CLASS software. This code makes the simplifying assumption that all hyperfine transitions within a given rotational transition share the same excitation temperature. For optically thin emission, the measured line ratios thus depend solely on the relative line strengths, which scale as the product $g_u A_{ul}$ (where g_u and A_{ul} are the degeneracy of the upper hyperfine level and Einstein coefficient of the hyperfine transition, respectively). In addition to obtaining hyperfine component intensity measurements, simultaneously fitting all hyperfine components results in determinations of the opacity and excitation temperature of the rotational transition. Fig. 5 and Table 4 summarize the results of this analysis for the APEX measurements of CN and C_2H line emission from TW Hya. The derived values of τ and T_{ex} are listed in Table 5.

Determination of column densities for hyperfine structures requires special care (see, e.g., Thi et al. 2004). In particular, the total partition function Q_{tot} must include the nuclear-spin statistics. In the case of the CN radical, this results in a factor 6 increase in Q_{tot} due to the $I = 1$ nuclear spin of the N atom and the $S = 1/2$ spin of the unpaired electron (Skatrud et al. 1983). The C_2H radical also has a $^2\Sigma^+$ ground electronic state, hence presenting a spin-rotation splitting, which further couples with the nuclear spin of the H atom (Müller

et al. 2000), such that the total partition function is 4 times the rotational partition function. The column density is then computed as

$$N_{\text{tot}} = \frac{8\pi\nu^3}{c^3} \frac{e^{E_l/kT_{\text{ex}}}}{1 - e^{-T_{ul}/T_{\text{ex}}}} \int \tau_{ul} dv \times \frac{Q_{\text{tot}}(T_{\text{ex}})}{A_{ul}g_u} \quad (5)$$

where all parameters refer to the particular hyperfine transition of interest. The beam-dilution correction (see Eq. 1) is applied to the spectrum before the HFS fitting procedure is performed. As for the column density estimates for ^{13}CO , HCN, and CS (§3.3), we adopt a beam dilution correction factor $f_{\text{dilution}} = 0.25$, although the results are relatively insensitive to the assumed source solid angle; e.g., assuming a C_2H source radius that is smaller by a factor of 2 results in a factor ~ 2 increase in T_{ex} (for CN, the value of T_{ex} is even less dependent on source solid angle). Following this procedure, we obtain estimates of $N_{\text{tot}}(\text{CN}) \sim 10^{14} \text{ cm}^{-2}$ and $N_{\text{tot}}(\text{C}_2\text{H}) \sim 5 \times 10^{15} \text{ cm}^{-2}$ for the TW Hya disk (Table 5). The former estimate is somewhat larger than that obtained by Thi et al. (2004), who based their results on a single CN hyperfine transition and assumed $T_{\text{ex}} = 25 \text{ K}$ (see §4).

3.4.2. V4046 Sgr

In the spectrum of V4046 Sgr, only the brighter components of the CN and C_2H hyperfine structure lines are detected (the detected components are displayed in the top panels of Fig. 3). Furthermore — as is evident from the comparison with TW Hya in Fig. 3 — these bright hyperfine components are blended, as a consequence of the V4046 Sgr disk’s broadened, double-peaked line profiles. We attempted to estimate intensities for the combined fluxes of the brightest hyperfine components by fitting a two-component Keplerian line profile model, in which the free parameters are the peak temperature of the brighter component and the component line ratio. The resulting total line intensities are listed in Table 4, and the two-component fit to the 340.04 GHz hyperfine complex of CN is displayed in Fig. 6. Even in this case, where the line blending is apparent in the observed profile, the data are sufficiently noisy that the line ratio is poorly constrained. Hence, in contrast to TW Hya, we cannot confidently determine the range of τ and T_{ex} characterizing the CN and C_2H emission from V4046 Sgr. However, we note that the results for the blended line intensities in these brighter hyperfine components suggest that the CN and C_2H emission is optically thin and thick, respectively. That is, whereas the CN line ratios are consistent with the theoretically predicted ratios (Table 4), the ratio of the two main C_2H component line complexes is consistent with nearly equal line intensities among the hyperfine components. The latter result suggests that we can estimate the excitation temperature of C_2H from its peak measured main-beam antenna temperature. Adopting the same correction for beam

dilution as applied in the case of TW Hya (i.e., $f_{\text{dilution}} = 0.25$), and accounting for the cosmic microwave background, we estimate $T_{\text{ex}} \sim 4$ K, i.e., very similar to the (low) T_{ex} value determined for TW Hya via analysis of its C_2H hyperfine emission (§3.4.1; Table 5).

As we have only limited information concerning τ and T_{ex} for CN and C_2H in the case of V4046 Sgr, we can only obtain order-of-magnitude estimates for the column densities for these species. Scaling the results for TW Hya (Table 5) according to the relative integrated line intensities, under the assumption that τ and T_{ex} are similar for the two disks, we crudely estimate $N_{\text{tot}}(\text{CN}) \sim 10^{14} \text{ cm}^{-2}$ and $N_{\text{tot}}(\text{C}_2\text{H}) \sim 10^{16} \text{ cm}^{-2}$ for V4046 Sgr. The former is likely an upper limit since, in the case of V4046 Sgr, the CN lines are evidently not optically thick.

3.5. Line ratios of isotopologues of CO: opacity diagnostics

Based on the sharp departures of measured $^{13}\text{CO}:^{12}\text{CO}$ line ratios from the canonical $^{13}\text{C}:^{12}\text{C}$ isotopic ratio determined for the solar neighborhood, Kastner et al. (1997) and Thi et al. (2004) had previously estimated $^{12}\text{CO}(3-2)$ emission line optical depths in the range $\tau_{12\text{CO}} \sim 10$ for TW Hya; Kastner et al. (2008) similarly estimated $\tau_{12\text{CO}} \sim 30$ for V4046 Sgr, based on measurements of the $J = 2 \rightarrow 1$ transitions of ^{13}CO and ^{12}CO . However, these estimates rely on the assumption that emission from ^{13}CO is optically thin. The measurements of $\text{C}^{18}\text{O}(2-1)$ and $(3-2)$ emission from the TW Hya disk in Qi et al. (2013b) and Table 1 provide a test of this assumption since, under the assumption of identical ^{13}CO and C^{18}O excitation temperatures,

$$R = \frac{1 - \exp(-\tau_{13\text{CO}})}{1 - \exp(-\tau_{13\text{CO}}/X)}, \quad (6)$$

where R is the measured $^{13}\text{CO}:\text{C}^{18}\text{O}$ line ratio and X is the $^{13}\text{CO}:\text{C}^{18}\text{O}$ abundance ratio. The latter quantity can be obtained from the ratio of isotopic ratios, i.e., $^{13}\text{C}:^{12}\text{C}/^{18}\text{O}:^{16}\text{O}$. We adopt $X = 7$, based on the values $^{12}\text{C}:^{13}\text{C} = 68$ and $^{16}\text{O}:^{18}\text{O} = 480$ (as determined from measurements of CN and CO lines for the local interstellar medium and Sun, respectively; Milam et al. 2005; Scott et al. 2006). Hence, in the optically thin limit ($\tau_{13\text{CO}} \ll 1$), we expect $R \approx 7$. The measured ratios for the $J = 2 \rightarrow 1$ and $J = 3 \rightarrow 2$ transitions for TW Hya ($R \approx 4.0$ and $R \approx 2.0$, respectively; Table 1), therefore imply the emission in the $^{13}\text{CO}(2-1)$ and $(3-2)$ lines is optically thick, with implied optical depths of $\tau_{13\text{CO}} \sim 1.5$ and $\tau_{13\text{CO}} \sim 5$, respectively.

Given the foregoing assumption for the isotopic abundances of carbon, we further expect $\tau_{12\text{CO}} \approx 68\tau_{13\text{CO}}$. Hence, it appears that previous single-dish-based determinations of $\tau_{12\text{CO}}$

for TW Hya are severe underestimates. If both $^{12}\text{CO}(3-2)$ and $^{13}\text{CO}(3-2)$ are indeed optically thick, then the mere factor ~ 7 difference in their integrated line intensities (Table 1) could reflect the fact that the (optically thicker) ^{12}CO emission arises from higher, warmer disk layers than the ^{13}CO . It is also likely, however, that the implicit assumption of uniform ^{13}CO optical depth over the disk surface is an oversimplification. We further note that our upper limit on $\text{C}^{18}\text{O}(3-2)$ emission from V4046 Sgr suggests $^{13}\text{CO}:\text{C}^{18}\text{O} > 2$, which would imply $\tau_{^{13}\text{CO}} < 5$ for V4046 Sgr in the $J = 3 \rightarrow 2$ transition — a surprising result, given the previous indications that ^{12}CO emission from TW Hya is, if anything, more optically thick than that from V4046 Sgr. The contrast in CO optical depths between the TW Hya and V4046 Sgr disks may be related to different outer disk density structures and/or outer radii, as the TW Hya molecular disk is somewhat smaller than the disk orbiting V4046 Sgr (respective radii ~ 200 AU and ~ 350 AU; Andrews et al. 2012; Rosenfeld et al. 2013). The two disks also have sharply contrasting disk structures on radial scales < 50 AU (i.e., $< 1''$), but such small-scale differences are unimportant for our single-dish ($\sim 20''$ beam diameter) CO measurements. Clearly, sensitive interferometric observations of ^{13}CO and C^{18}O toward both disks are warranted (see also discussion in Qi et al. 2013b).

4. Discussion

In Table 6, we list fractional molecular abundances relative to ^{13}CO , $N(\text{X})/N(^{13}\text{CO})$, obtained from the determinations of source-averaged molecular column densities for TW Hya and V4046 Sgr described in §3.4 and listed in Tables 3 and 5. These values of $N(\text{X})/N(^{13}\text{CO})$ were obtained by adopting $T_{\text{ex}} = 18.75$ K for ^{13}CO (based on recent modeling of the TW Hya and V4046 Sgr disks; Rosenfeld et al. 2013; Bergin et al. 2013) as well as for HCN and CS, and $T_{\text{ex}} = 10$ K and 5 K for CN and C_2H , respectively (Table 5). Table 6 also lists values of $N(\text{X})/N(^{13}\text{CO})$ based on results previously obtained for the disks orbiting the T Tauri stars LkCa 15 and DM Tau as well as for the deeply embedded (candidate “Class 0”), low-mass protostars R CrA IRS 7B and IRAS 16293–2422. To our knowledge, these four objects are the only other low-mass, pre-main sequence stars and protostars for which molecular line surveys encompassing all five of the molecules in Tables 3 and 5 have been reported in the literature. Both of the protostars are classified as “hot corinos,” i.e., protostellar envelopes that are particularly chemically active due to strong heating from accretion processes and/or external radiation fields (e.g., Bottinelli et al. 2007; Watanabe et al. 2012). Table 6 also includes fractional molecular abundances measured for the planetary nebula NGC 7027, which features strong stellar UV and nebular X-ray radiation fields (see, e.g., Kastner et al. 2012).

The comparison of $N(\text{X})/N(^{13}\text{CO})$ values in Table 6 indicates that the fractional CN and C_2H abundances in the evolved disks orbiting the “old” (age $\sim 8\text{--}20$) Myr-old T Tauri stars TW Hya and V4046 Sgr are strongly (factors $\sim 30\text{--}1000$) enhanced over those characteristic of the other chemically rich object classes represented in the Table; C_2H appears to be even more abundant in the TW Hya and V4046 Sgr disks than in the somewhat younger (age $3\text{--}5$ Myr) T Tauri star/disk systems LkCa 15 and DM Tau. We caution that the apparent sharp contrast in the ratios $N(\text{CN})/N(^{13}\text{CO})$ and (especially) $N(\text{C}_2\text{H})/N(^{13}\text{CO})$ that are listed in Table 6 may be due, at least in part, to different assumptions regarding the beam filling factors and optical depths of emission from the various molecular species in these sources, as well as to the variety of methods used to deduce T_{ex} for purposes of calculating the values of N . Nevertheless, this comparison between disks, “hot corinos,” and UV/X-ray-luminous planetary nebula supports previous suggestions (Kastner et al. 1997, 2008; Dutrey et al. 1997; Thi et al. 2004; Henning et al. 2010) that high-energy (FUV and/or X-ray) radiation from the vicinity of the central stars is enhancing the abundances of CN and C_2H in T Tauri disks. Similar inferences concerning the likely influence of X-rays on disk chemistry were drawn by Kastner et al. (2008), Thi et al. (2004), and Salter et al. (2011) on the basis of enhanced HCN and HCO^+ line fluxes from T Tauri disks. Our tentative determinations of low T_{ex} ($\sim 5\text{--}10$ K) for CN in TW Hya and for C_2H in both TW Hya and V4046 Sgr (§3.4) — which are consistent with inferences concerning T_{ex} for these two species in the DM Tau and LkCa 15 disks (Henning et al. 2010; Chapillon et al. 2012) — may indicate that the mm-wave emission from CN and C_2H arises from regions that are rather deep within the disks. If so, it would then stand to reason that the abundances of C_2H and, perhaps, CN are being enhanced by X-rays rather than by FUV photons, given that X-rays can penetrate to much larger column densities within the disk (e.g., Skinner & Guedel 2013; Cleeves, Adams, & Bergin 2013).

Indeed, all four stars considered here are relatively luminous X-ray sources — with $L_X \approx 10^{30}$ erg s $^{-1}$ in each case — based on published X-ray studies for TW Hya (Kastner et al. 2002), V4046 Sgr (Günther et al. 2006), and LkCa 15 (Skinner & Güdel 2013), and archival X-ray data for DM Tau (which was detected serendipitously by Chandra). Furthermore, the similarly evolved (age ~ 5 Myr) molecular disk orbiting another X-ray-luminous T Tauri star, T Cha, also appears to show enhanced CN and HCN emission (Sacco et al. 2014, note that C_2H has yet to be measured for the T Cha disk). The intrinsic X-ray spectral energy distributions of the central stars of the four evolved T Tauri star/disk systems that have been studied in detail thus far (TW Hya, V4046 Sgr, LkCa 15, and T Cha) appear similar to each other, with contributions from both relatively soft (~ 3 MK, accretion shock) and somewhat harder (~ 10 MK, coronal) components. This combination likely leads to a very large range of X-ray photon penetration depths within the disk (Skinner & Güdel 2013), enhancing

molecular ionization and dissociation rates and perhaps increasing the abundances of species, like C_2H , that are the dissociation products of more complex organic molecules. These disk irradiation effects then may be reinforced by dust grain surface chemistry processes that favor enhanced production of organic molecules deep within disks (Walsh et al. 2014).

On the other hand, simulations by Walsh et al. (2012) indicate that disk CN and C_2H abundances are not very sensitive to X-ray irradiation. This raises the possibility that these species are subthermally excited in the disk, as a consequence of their large column densities and (hence) large optical depths (Table 5); the resulting “photon trapping” would effectively lower the critical densities for excitation. Interferometric imaging of the TW Hya and V4046 Sgr disks in lines of CN and C_2H that can elucidate the radial and vertical distributions of these species within the disk will be required to distinguish between irradiation and other mechanisms that might enhance their relative abundances.

5. Conclusions

We have used the APEX 12 m telescope and broad-band spectrometer to conduct comprehensive mm-wave molecular emission line surveys of the evolved circumstellar disks orbiting the nearby, evolved T Tauri stars TW Hya and V4046 Sgr AB over the frequency range 275–357 GHz. We find that lines of ^{12}CO , ^{13}CO , HCN, CN, and C_2H constitute the strongest molecular emission from both disks in this spectral region. The molecule C_2H is detected here for the first time in both disks, as is CS in the TW Hya disk. The survey results also include the first measurements of the full suite of hyperfine transitions of CN $N = 3 \rightarrow 2$ and C_2H $N = 4 \rightarrow 3$ in both disks. Modeling of these CN and C_2H hyperfine complexes in the spectrum of TW Hya indicates that the emission from both species is optically thick and suggests either that emission from CN and C_2H originates from very cold ($\lesssim 10$ K) regions, or that these molecules are subthermally excited. The former possibility, if confirmed, would suggest efficient production of CN and C_2H in the outer disk and/or near the disk midplane. It furthermore appears that the fractional abundances of CN and, especially, C_2H are significantly enhanced in these evolved protoplanetary disks relative to the fractional abundances of the same molecules in the environments of deeply embedded protostars.

Clearly, additional work will be necessary to understand the various molecular abundance anomalies apparent in evolved disks orbiting relatively “old” T Tauri stars. In this regard, several lines of research are warranted: molecular line surveys of additional disks representing a wider range of evolutionary states; interferometric imaging of the T Tauri star disks in Table 6 (as well as T Cha) in lines of CN, C_2H , and other potential molec-

ular tracers of X-irradiation at high sensitivity and angular resolution (i.e., with ALMA); and detailed numerical simulations of these same systems with an irradiated disk model that incorporates key, observationally-constrained star/disk system parameters — such as specific incident stellar FUV and X-ray radiation fields, as well as disk masses, radii, gas compositions, gas-to-dust ratios, and viewing angles.

This publication is based on data acquired with the Atacama Pathfinder Experiment (APEX). APEX is a collaboration between the Max-Planck-Institut für Radioastronomie, the European Southern Observatory, and the Onsala Space Observatory. The authors gratefully acknowledge illuminating discussions with Uma Gorti, Karin Oberg, Charlie Qi, and David Wilner, as well as incisive comments from the anonymous referee, all of which significantly improved this paper. This research is supported by National Science Foundation grant AST-1108950 to RIT. D.R.R. acknowledges support from Chilean FONDECYT grant 3130520.

REFERENCES

- Andrews, S. M., et al. 2012, *ApJ*, 744, 162
- Aresu, G., Meijerink, R., Kamp, I., Spaans, M., Thi, W.-F., & Woitke, P. 2012, *A&A*, 547, A69
- Bergin, E. A., et al. 2013, *Nature*, 493, 644
- Binks, A. S., & Jeffries, R. D. 2014, *MNRAS*, 438, L11
- Blake, G. A., Masson, C. R., Phillips, T. G., & Sutton, E. C. 1986, *ApJS*, 60, 357
- Blake, G. A., van Dishoeck, E. F., Jansen, D. J., Groesbeck, T. D., & Mundy, L. G. 1994, *ApJ*, 428, 680
- Bottinelli, S., Ceccarelli, C., Williams, J. P., & Lefloch, B. 2007, *A&A*, 463, 601
- Caux, E., et al. 2011, *A&A*, 532, A23
- Chapillon, E., Guilloteau, S., Dutrey, A., Piétu, V., & Guélin, M. 2012, *A&A*, 537, A60
- Chapillon, E., Parise, B., Guilloteau, S., & Du, F. 2011, *A&A*, 533, A143
- Cleeves, L. I., Adams, F. C., & Bergin, E. A. 2013, *ApJ*, 772, 5
- Drake, J. J., Ercolano, B., Flaccomio, E., & Micela, G. 2009, *ApJ*, 699, L35

- Ducourant, C., Teixeira, R., Galli, P. A. B., Le Campion, J. F., Krone-Martins, A., Zuckerman, B., Chauvin, G., & Song, I. 2014, *A&A*, 563, A121
- Dutrey, A., Guilloteau, S., & Guelin, M. 1997, *A&A*, 317, L55
- Dutrey, A., et al. 2014, ArXiv e-prints
- Ehrenfreund, P., & Charnley, S. B. 2000, *ARA&A*, 38, 427
- Ercolano, B., Clarke, C. J., & Drake, J. J. 2009, *ApJ*, 699, 1639
- Ercolano, B., Drake, J. J., Raymond, J. C., & Clarke, C. C. 2008, *ApJ*, 688, 398
- Glassgold, A. E., Galli, D., & Padovani, M. 2012, *ApJ*, 756, 157
- Glassgold, A. E., Meijerink, R., & Najita, J. R. 2009, *ApJ*, 701, 142
- Glassgold, A. E., Najita, J., & Igea, J. 1997, *ApJ*, 480, 344
- . 2004, *ApJ*, 615, 972
- Goldsmith, P. F., & Langer, W. D. 1999, *ApJ*, 517, 209
- Gorti, U., Dullemond, C. P., & Hollenbach, D. 2009, *ApJ*, 705, 1237
- Gorti, U., & Hollenbach, D. 2008, *ApJ*, 683, 287
- Gorti, U., Hollenbach, D., Najita, J., & Pascucci, I. 2011, *ApJ*, 735, 90
- Günther, H. M., Liefke, C., Schmitt, J. H. M. M., Robrade, J., & Ness, J.-U. 2006, *A&A*, 459, L29
- Hasegawa, T. I., & Kwok, S. 2001, *ApJ*, 562, 824
- Henning, T., et al. 2010, *ApJ*, 714, 1511
- Hubbard, W. B., Burrows, A., & Lunine, J. I. 2002, *ARA&A*, 40, 103
- Johansson, L. E. B., et al. 1984, *A&A*, 130, 227
- Kaifu, N., et al. 2004, *PASJ*, 56, 69
- Kastner, J. H., Huenemoerder, D. P., Schulz, N. S., Canizares, C. R., & Weintraub, D. A. 2002, *ApJ*, 567, 434
- Kastner, J. H., Zuckerman, B., Hily-Blant, P., & Forveille, T. 2008, *A&A*, 492, 469

- Kastner, J. H., Zuckerman, B., Weintraub, D. A., & Forveille, T. 1997, *Science*, 277, 67
- Kastner, J. H., et al. 2012, *AJ*, 144, 58
- Klein, B., Philipp, S. D., Krämer, I., Kasemann, C., Güsten, R., & Menten, K. M. 2006, *A&A*, 454, L29
- Luu, J. X., & Jewitt, D. C. 2002, *ARA&A*, 40, 63
- Meijerink, R., Glassgold, A. E., & Najita, J. R. 2008, *ApJ*, 676, 518
- Milam, S. N., Savage, C., Brewster, M. A., Ziurys, L. M., & Wyckoff, S. 2005, *ApJ*, 634, 1126
- Müller, H. S. P., Klaus, T., & Winnewisser, G. 2000, *A&A*, 357, L65
- Öberg, K. I., Qi, C., Wilner, D. J., & Hogerheijde, M. R. 2012, *ApJ*, 749, 162
- Öberg, K. I., et al. 2011, *ApJ*, 734, 98
- Owen, J. E., Ercolano, B., & Clarke, C. J. 2011, *MNRAS*, 412, 13
- Owen, J. E., Ercolano, B., Clarke, C. J., & Alexander, R. D. 2010, *MNRAS*, 401, 1415
- Pety, J. 2005, in *SF2A-2005: Semaine de l’Astrophysique Francaise*, ed. F. Casoli, T. Contini, J. M. Hameury, & L. Pagani, 721
- Qi, C., Öberg, K. I., & Wilner, D. J. 2013a, *ApJ*, 765, 34
- Qi, C., Wilner, D. J., Aikawa, Y., Blake, G. A., & Hogerheijde, M. R. 2008, *ApJ*, 681, 1396
- Qi, C., Wilner, D. J., Calvet, N., Bourke, T. L., Blake, G. A., Hogerheijde, M. R., Ho, P. T. P., & Bergin, E. 2006, *ApJ*, 636, L157
- Qi, C., et al. 2004, *ApJ*, 616, L11
- . 2013b, *Science*, 341, 630
- Rodriguez, D. R., Kastner, J. H., Wilner, D., & Qi, C. 2010, *ApJ*, 720, 1684
- Rosenfeld, K. A., Andrews, S. M., Wilner, D. J., Kastner, J. H., & McClure, M. K. 2013, *ApJ*, 775, 136
- Rosenfeld, K. A., Andrews, S. M., Wilner, D. J., & Stempels, H. C. 2012a, *ApJ*, 759, 119
- Rosenfeld, K. A., et al. 2012b, *ApJ*, 757, 129

- Sacco, G. G., Kastner, J. H., Forveille, T., Principe, D., Montez, R., Zuckerman, B., & Hily-Blant, P. 2014, *A&A*, 561, A42
- Salter, D. M., Hogerheijde, M. R., van der Burg, R. F. J., Kristensen, L. E., & Brinch, C. 2011, *A&A*, 536, A80
- Schilke, P., Groesbeck, T. D., Blake, G. A., & Phillips, T. G. 1997, *ApJS*, 108, 301
- Schöier, F. L., Jørgensen, J. K., van Dishoeck, E. F., & Blake, G. A. 2002, *A&A*, 390, 1001
- Scott, P. C., Asplund, M., Grevesse, N., & Sauval, A. J. 2006, *A&A*, 456, 675
- Skatrud, D. D., de Lucia, F. C., Blake, G. A., & Sastry, K. V. L. N. 1983, *Journal of Molecular Spectroscopy*, 99, 35
- Skinner, S. L., & Güdel, M. 2013, *ApJ*, 765, 3
- Stäuber, P., Doty, S. D., van Dishoeck, E. F., & Benz, A. O. 2005, *A&A*, 440, 949
- Thi, W., van Zadelhoff, G., & van Dishoeck, E. F. 2004, *A&A*, 425, 955
- Torres, C. A. O., Quast, G. R., Melo, C. H. F., & Sterzik, M. F. 2008, *Young Nearby Loose Associations*, ed. Reipurth, B., 757–+
- van Dishoeck, E. F., Blake, G. A., Jansen, D. J., & Groesbeck, T. D. 1995, *ApJ*, 447, 760
- Walsh, C., Millar, T. J., Nomura, H., Herbst, E., Widicus Weaver, S., Aikawa, Y., Laas, J. C., & Vasyunin, A. I. 2014, *A&A*, 563, A33
- Walsh, C., Nomura, H., Millar, T. J., & Aikawa, Y. 2012, *ApJ*, 747, 114
- Watanabe, Y., Sakai, N., Lindberg, J. E., Jørgensen, J. K., Bisschop, S. E., & Yamamoto, S. 2012, *ApJ*, 745, 126
- Williams, J. P., & Cieza, L. A. 2011, *ARA&A*, 49, 67
- Ziurys, L. M., Saykally, R. J., Plambeck, R. L., & Erickson, N. R. 1982, *ApJ*, 254, 94

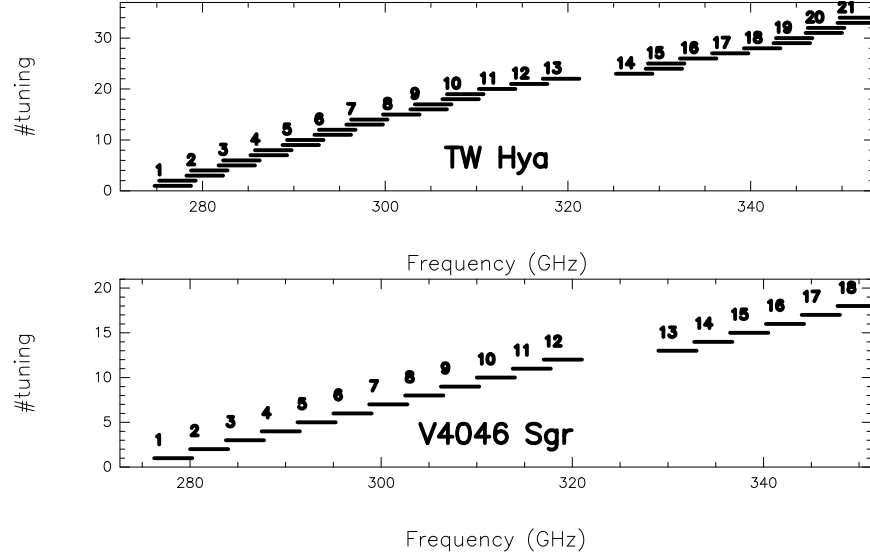


Fig. 1.— APEX XFFTS2 spectral coverage for the TW Hya (top) and V4046 Sgr (bottom) spectral surveys.

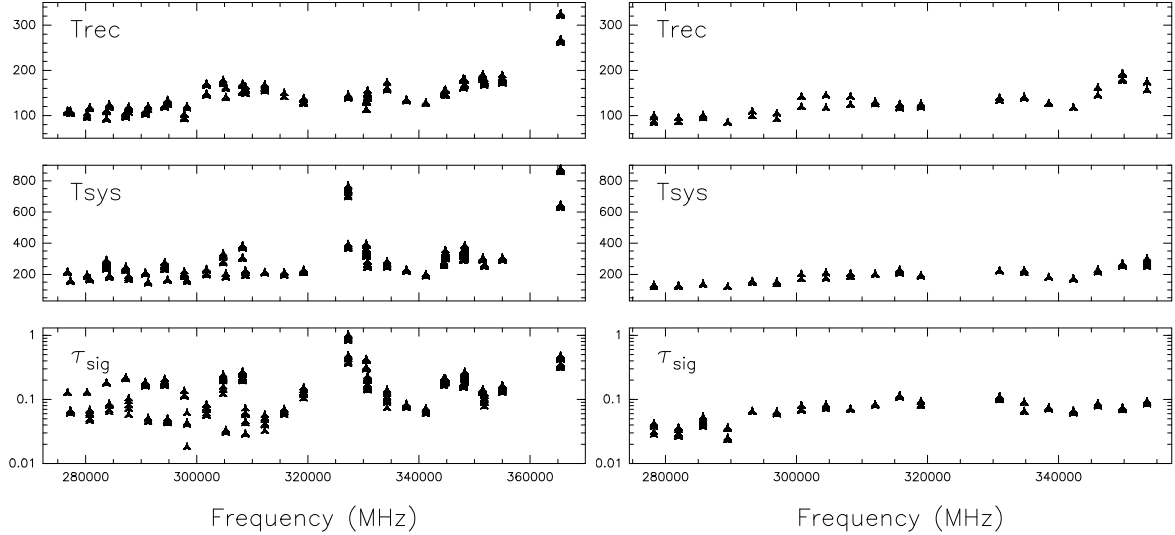


Fig. 2.— Receiver temperatures (top), system temperatures (middle), and signal-band opacities (bottom) as functions of frequency during the TW Hya (left) and V4046 Sgr (right) spectral surveys.

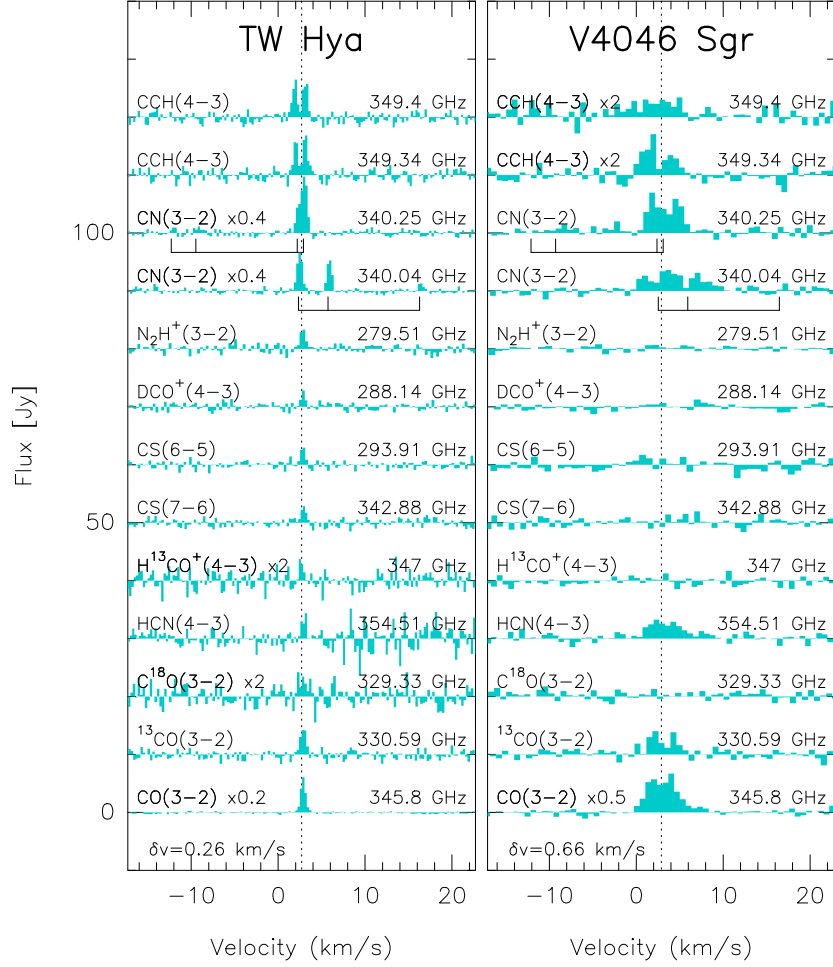


Fig. 3.— Spectra of all molecular transitions that are well detected in the merged 0.8 mm band APEX spectrum of TW Hya (left), and the same transitions for V4046 Sgr (right). Ordinate is velocity with respect to the local standard of rest and abscissa is line flux (in Jy); for clarity, spectral regions (other than ^{12}CO) have been shifted upwards, and some lines have been rescaled. The strongest molecular lines include C_2H , which is detected here for the first time in both disks (§3.2).

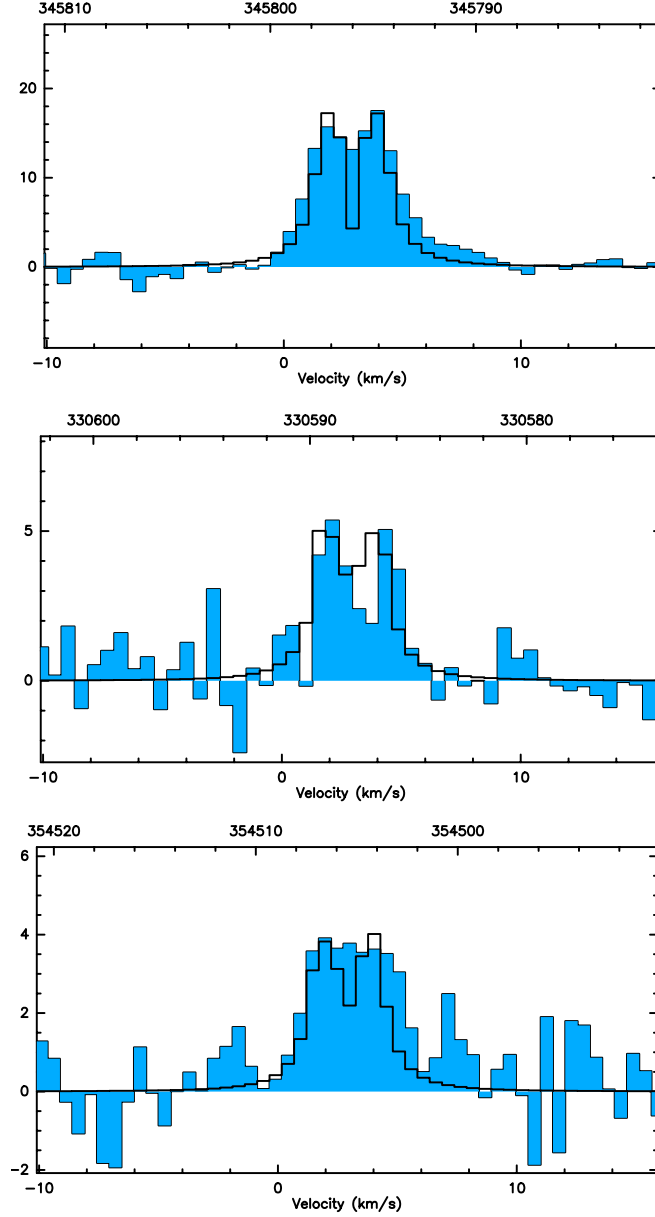


Fig. 4.— APEX spectra of newly observed (330-354 GHz) transitions of molecular species previously detected in V4046 Sgr (blue histograms) overlaid with parametric Keplerian model line profiles (see §3.2.2). In each panel, ordinate is velocity with respect to the local standard of rest (with frequencies in MHz at the top of each panel) and abscissa is line flux in Jy. From top to bottom: CO ($J = 3 \rightarrow 2$), ^{13}CO ($J = 3 \rightarrow 2$), and HCN ($J = 4 \rightarrow 3$).

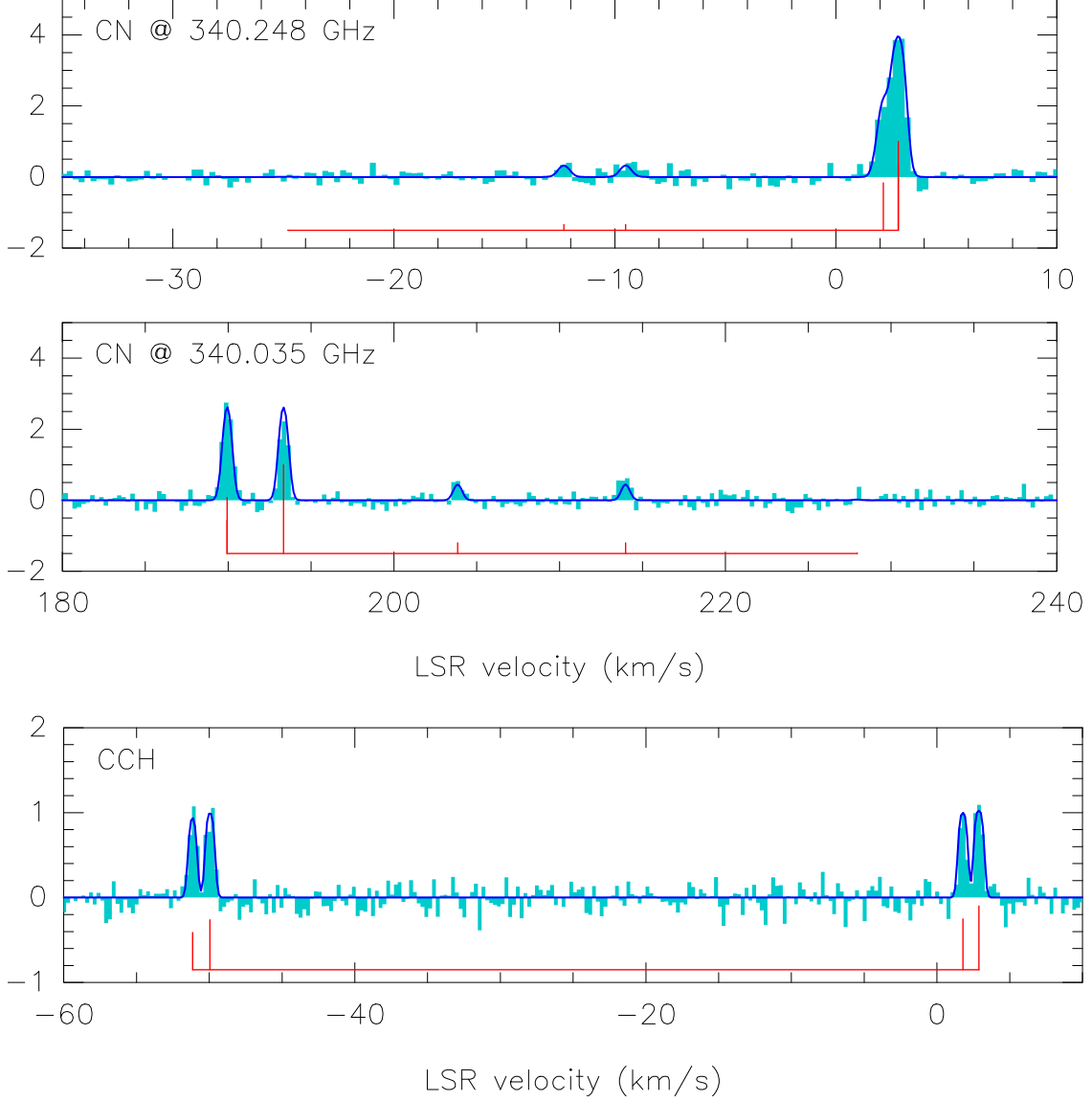


Fig. 5.— Full spectra of hyperfine components of CN (top and middle panels) and C_2H (bottom panel) observed toward TW Hya. The red lines indicate the positions and relative intensities of the hyperfine components (see Table 4). The spectra are overlaid with the best-fit models obtained via the method described in §3.4. The intensity scale (in K) has been corrected for beam efficiency and beam dilution.

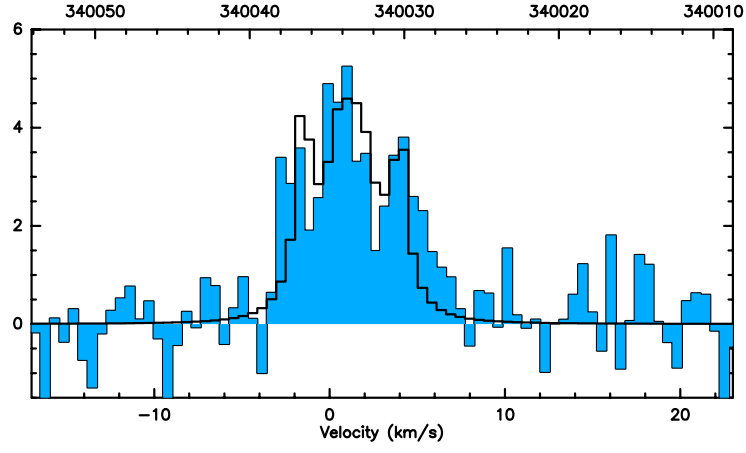


Fig. 6.— Spectrum of 340.04 GHz CN ($N = 3 \rightarrow 2$) emission from the V4046 Sgr disk, with best-fit multiple-component parametric Keplerian line profile overlaid (see §3.4.2). Ordinate is velocity with respect to the local standard of rest (with corresponding frequencies in MHz labeled across the top of the panel) and abscissa is line flux (in Jy).

Table 1: TW HYA & V4046 SGR: MOLECULAR SPECIES AND TRANSITIONS DETECTED^a
BY APEX

Species	Trans.	ν	E_u/k	A_{ul}	μ	I (Jy km s ⁻¹)	
		(GHz)	(K)	(s ⁻¹)	(Debye)	TW Hya	V4046 Sgr
¹² CO	$J = 3 \rightarrow 2$	345.7960	21.3 (0.3)	66.3 (2.2)
¹³ CO	$J = 3 \rightarrow 2$	330.5881	31.7319	2.199×10^{-6}	0.11046	4.02 (0.40)	19.6 (1.4)
C ¹⁸ O	$J = 3 \rightarrow 2$	329.3305	2.0 ^b	<10
C ₂ H	$N = 4 \rightarrow 3$	349.34–349.40	41.9148	1.411×10^{-4}	0.8	10.8 ^c	22.8 ^c
CN	$N = 3 \rightarrow 2$	340.03–340.26	32.6280	4.123×10^{-4}	1.45	51.3 ^c	54.0 ^c
HCN	$J = 4 \rightarrow 3$	354.505476	42.5348	2.047×10^{-3}	2.98	4.92 (0.81)	14.6 (0.8)
N ₂ H ⁺	$J = 3 \rightarrow 2$	279.512	2.87 (0.41)	<5
DCO ⁺	$J = 4 \rightarrow 3$	288.144	1.64 (0.28)	<5
CS	$J = 6 \rightarrow 5$	293.912244	49.3717	5.240×10^{-4}	1.96	2.26 (0.28)	<14
	$J = 7 \rightarrow 6$	342.88300	2.39 (0.31)	<8
H ¹³ CO ⁺	$J = 4 \rightarrow 3$	346.9983	1.2 ^b	<5

a) Upper limits are 3σ .

b) Measured line intensity has a large uncertainty.

c) Sum of integrated intensities of hyperfine structure lines (with estimated uncertainties $\sim 10\%$); see Table 4.

Table 2. MOLECULAR SPECIES DETECTED^a TOWARD TW Hya AND/OR V4046 Sgr, 215–373 GHz

Species	Trans.	ν (GHz)	TW Hya		V4046 Sgr	
			I^b (Jy km s ⁻¹)	Refs. ^c	I (Jy km s ⁻¹)	Refs. ^c
¹² CO	$J = 2 \rightarrow 1$	230.5380	15.9	2	17.3, 20.0, 34.5	7, 8, 9
	$J = 3 \rightarrow 2$	345.7960	21.3, 29.8, 30.9	1, 2, 3	66.3	1
¹³ CO	$J = 2 \rightarrow 1$	220.3987	2.2, 2.7	2, 4	9.1, 9.4	7, 9
	$J = 3 \rightarrow 2$	330.5881	4.0, 3.7	1, 3	19.6	1
C ¹⁸ O	$J = 2 \rightarrow 1$	219.560	0.68	4	0.6 ^d	9
	$J = 3 \rightarrow 2$	329.3305	2.1 ^d	1	<10	1
C ₂ H	$N = 4 \rightarrow 3$	349.338	5.4 ^e	1	12.2 ^e	1
	$J = 3 \rightarrow 2$	349.399	5.2 ^e	1	10.6 ^e	1
CN	$N = 2 \rightarrow 1$	226.6794	...		1.29	8
		226.8747	...		17.7, 12.0	7, 8
	$N = 3 \rightarrow 2$	340.0315	24.2 ^e , 12.5 ^e	1, 2	22.6 ^e	1
		340.2478	27.1 ^e , 18.7 ^e , 17.8 ^e	1, 2, 3	31.4 ^e	1
HCN	$J = 3 \rightarrow 2$	265.8864	7.0	2	10.3, 9.9	7, 8
	$J = 4 \rightarrow 3$	354.505476	4.9, 8.3, 7.6	1, 2, 3	14.6	1
DCN	$J = 3 \rightarrow 2$	217.2386	... <i>f</i>		<0.38	8
	$J = 5 \rightarrow 4$	362.046	<0.5	3	...	
H ¹³ CN	$J = 4 \rightarrow 3$	345.339	<0.9, <0.6	1, 3	<5	1
HNC	$J = 4 \rightarrow 3$	362.630	<0.8	3	...	
HCO ⁺	$J = 3 \rightarrow 2$	267.557625	... <i>f</i>		11.3, 11.43	7, 8
	$J = 4 \rightarrow 3$	356.73425	21.8, 19.7	2, 3	...	
DCO ⁺	$J = 3 \rightarrow 2$	216.1126	... <i>f</i>		0.80	8
	$J = 4 \rightarrow 3$	288.144	1.6	1	<5	1
	$J = 5 \rightarrow 4$	360.169	1.7	3	...	
H ¹³ CO ⁺	$J = 4 \rightarrow 3$	346.998	1.2 ^d , 1.1	1, 3	<5	1
N ₂ H ⁺	$J = 3 \rightarrow 2$	279.512	2.9, 2.6, 2.2	1, 4, 5	<5, 2.6	1, 8
	$J = 4 \rightarrow 3$	372.672	<5	3	...	

Table 2—Continued

Species	Trans.	ν (GHz)	TW Hya		V4046 Sgr	
			I^b (Jy km s ⁻¹)	Refs. ^c	I (Jy km s ⁻¹)	Refs. ^c
CS	$J = 6 \rightarrow 5$	293.912244	2.3	1	<14	1
	$J = 7 \rightarrow 6$	342.88300	2.4	1	<8	1
H ₂ CO	$J = 3 \rightarrow 2$	225.697	<0.8	3	1.01	8
	$J = 4 \rightarrow 3$	281.5269	<2.5, 1.2	1, 5	<5, 0.95	1, 8
		300.8366	<2.5	1	<5	1
	$J = 5 \rightarrow 4$	351.768	<0.6, 0.54	3, 5	<5	1
CO ⁺	$N = 3 \rightarrow 2$	354.0142	<2.5	1	<10	1
SO	$J = 8 \rightarrow 7$	344.310	<2.5, <1.6	1, 3	<5	1
CH ₃ OH	$J = 7 \rightarrow 6$	338.409	<2.5, <0.3	1, 3	<5	1
H ₂ D ⁺	$J = 1 \rightarrow 1$	372.421	<1	6	...	

a) Selected species with transitions in this range that have not been detected in either disk are indicated in italics. Ellipses indicate transitions that are not covered by our line surveys and have yet to be measured in one of the two disks. Upper limits are 3σ apart from measurements by Thi et al. (2004), which are 2σ .

b) JCMT measurements from Kastner et al. (1997) and Thi et al. (2004) converted to Jy km s⁻¹ assuming a conversion of 15.6 Jy K⁻¹ (see http://docs.jach.hawaii.edu/JCMT/HET/GUIDE/het_guide.ps).

c) References: 1. this work; 2. Kastner et al. (1997); 3. Thi et al. (2004); 4. Qi et al. (2013b); 5. Qi et al. (2013a) 6. Chapillon et al. (2011); 7. Kastner et al. (2008); 8. Öberg et al. (2011); 9. Rosenfeld et al. (2013).

d) Measured line intensity is highly uncertain.

e) Integrated line intensities for hyperfine complexes centered at the listed frequencies (see Table 4).

f) Detections of the $J = 3 \rightarrow 2$ transitions of DCN and DCO⁺ were reported in Qi et al. (2008) and Öberg et al. (2012); detection of the $J = 3 \rightarrow 2$ transition of HCN was reported in Qi et al. (2008).

Table 3: TW Hya & V4046 Sgr: ^{13}CO , HCN, AND CS COLUMN DENSITIES^a

Species (Trans.)	T_{ex} (K)	$\log Q(T)$	TW Hya		V4046 Sgr	
			N_X (cm^{-2})	$N_X/N_{^{13}\text{CO}}$	N_X (cm^{-2})	$N_X/N_{^{13}\text{CO}}$
^{13}CO (3–2)	37.5	1.162	2.0×10^{14}	...	9.9×10^{14}	...
	18.75	0.871	2.4×10^{14}	...	1.2×10^{15}	...
	9.375	0.589	6.8×10^{14}	...	3.3×10^{15}	...
	5.0	0.347	7.5×10^{15}	...	3.7×10^{16}	...
HCN (4–3)	37.5	1.254	3.9×10^{11}	2.0×10^{-3}	1.2×10^{12}	1.2×10^{-3}
	18.75	0.961	6.2×10^{11}	2.6×10^{-3}	2.0×10^{12}	1.7×10^{-3}
	9.375	0.676	3.1×10^{12}	4.6×10^{-3}	9.8×10^{12}	3.0×10^{-3}
	5.0	0.429	9.3×10^{13}	0.012	2.9×10^{14}	7.8×10^{-3}
CS (6–5)	37.5	1.508	7.2×10^{11}	3.6×10^{-3}	$< 4.5 \times 10^{12}$	$< 4.5 \times 10^{-3}$
	18.75	1.212	1.4×10^{12}	5.8×10^{-3}	$< 8.4 \times 10^{12}$	$< 7.0 \times 10^{-3}$
	9.375	0.920	9.6×10^{12}	0.014	$< 6.0 \times 10^{13}$	< 0.18
	5.0	0.661	5.3×10^{14}	0.071	$< 3.8 \times 10^{15}$	< 0.10

a) Source-averaged column densities assuming optically thin emission and adopting source radii (for all molecules) of $5''$ for both disks. Upper limits for N_X values are based on 3σ upper limits for line intensities. See §3.4.

Table 4: TW Hya & V4046 Sgr: TRANSITIONS OF CN AND C₂H MEASURED BY APEX

Species (Rot. trans.)	Transition	ν^a (GHz)	A_{ul}^a (s ⁻¹)	g_u^a	R.I. ^a	TW Hya I (Jy km s ⁻¹)	V4046 Sgr I (Jy km s ⁻¹)
CN ($N = 3 \rightarrow 2$)	$J = 5/2 \rightarrow 3/2, F = 3/2 \rightarrow 5/2$	339.992257	3.89×10^{-6}	4	0.0009	0.04	...
	$J = 5/2 \rightarrow 3/2, F = 5/2 \rightarrow 5/2$	340.008126	6.20×10^{-5}	6	0.0218	1.59	...
	$J = 5/2 \rightarrow 3/2, F = 3/2 \rightarrow 3/2$	340.019626	9.27×10^{-5}	4	0.0217	1.10	...
	$J = 5/2 \rightarrow 3/2, F = 7/2 \rightarrow 5/2$	340.031549	3.85×10^{-4}	8	0.1801	10.4	22.6 ^b
	$J = 5/2 \rightarrow 3/2, F = 3/2 \rightarrow 1/2$	340.035408	2.89×10^{-4}	4	0.0676	3.11	...
	$J = 5/2 \rightarrow 3/2, F = 3/2 \rightarrow 1/2$	340.035408	3.23×10^{-4}	6	0.1135	6.60	...
	$J = 7/2 \rightarrow 5/2, F = 7/2 \rightarrow 5/2$	340.247770	3.80×10^{-4}	8	0.1778	10.3	31.6 ^c
	$J = 7/2 \rightarrow 5/2, F = 9/2 \rightarrow 7/2$	340.247770	4.13×10^{-4}	10	0.2419	12.5	...
	$J = 7/2 \rightarrow 5/2, F = 5/2 \rightarrow 3/2$	340.248544	3.67×10^{-4}	6	0.1290	7.22	...
	$J = 7/2 \rightarrow 5/2, F = 5/2 \rightarrow 5/2$	340.261773	4.48×10^{-5}	6	0.0157	1.19	...
	$J = 7/2 \rightarrow 5/2, F = 7/2 \rightarrow 7/2$	340.264949	3.35×10^{-5}	8	0.0157	1.56	...
	$J = 7/2 \rightarrow 5/2, F = 5/2 \rightarrow 7/2$	340.279120	9.27×10^{-7}	6	0.0003	0.04	...
C ₂ H ($N = 4 \rightarrow 3$)	$J = 9/2 \rightarrow 7/2, F = 5 \rightarrow 4$	349.337706	1.31×10^{-4}	11	0.3105	2.7	12 ^d
	$J = 9/2 \rightarrow 7/2, F = 4 \rightarrow 3$	349.338988	1.28×10^{-4}	9	0.2481	2.7	...
	$J = 7/2 \rightarrow 5/2, F = 4 \rightarrow 3$	349.399276	1.25×10^{-4}	9	0.2434	2.7	11 ^e
	$J = 7/2 \rightarrow 5/2, F = 4 \rightarrow 3$	349.400671	1.20×10^{-4}	7	0.1816	2.5	...

- a) Values of frequencies, A_{ul} , g_u , and theoretical relative intensities (R.I.) of hyperfine transitions of CN and C₂H obtained from JPL and CDMS databases, Müller et al. (2000), and Skatrud et al. (1983).
b) Sum of integrated intensities of hyperfine structure lines in range 340.032–340.035 GHz.
c) Sum of integrated intensities of hyperfine structure lines in range 340.248–340.249 GHz.
d) Sum of integrated intensities of hyperfine structure lines in range 349.338–349.339 GHz.
e) Sum of integrated intensities of hyperfine structure lines in range 349.399–349.400 GHz.

Table 5: RESULTS OF CN AND C₂H HYPERFINE STRUCTURE ANALYSIS FOR TW Hya

Species	v_0 (km s ⁻¹)	FWHM (km s ⁻¹)	τ^a	T_{ex} (K)	$N_{\text{tot}}/Q_{\text{tot}}^b$ (cm ⁻²)	$Q_{\text{tot}}(T_{\text{ex}})^c$	N_{tot}^d (cm ⁻²)
CN	2.80±0.10	0.61±0.02	4.7±0.6	10.8±0.8	3.7×10^{12}	25.9±1.5	$(9.6 \pm 1.0) \times 10^{13}$
C ₂ H	2.90±0.05	0.48±0.05	12.6±5.0	6.0±0.9	4.0×10^{14}	12.9±1.9	$(5.1 \pm 3.0) \times 10^{15}$

- a) Total opacity obtained as the sum of individual hyperfine line opacities τ_{ul} , where $\tau_{ul} = \text{R.I.} \times \tau$.
b) From Eq. 5.
c) From a linear interpolation to tabulated partition function values obtained from the CDMS database.
d) Column densities assuming a source radius of 5'' for both molecules. See §3.4.

Table 6: COMPARISON OF FRACTIONAL ABUNDANCES RELATIVE TO ^{13}CO , $N(\text{X})/N(^{13}\text{CO})$

MOLECULE	PROTOPLANETARY DISKS ^a				PROTOSTARS ^b		PN ^c
	TW Hya	V4046 Sgr	LkCa 15	DM Tau	IRS 7B	IRAS 16293	NGC 7027
HCN	2.6×10^{-3}	1.7×10^{-3}	5.0×10^{-3}	1.7×10^{-3}	6.6×10^{-4}	1.7×10^{-3}	1.0×10^{-4}
CS	5.8×10^{-3}	$< 7.0 \times 10^{-3}$	0.015	1.0×10^{-3}	1.7×10^{-3}	4.6×10^{-3}	...
CN	0.40	0.08^d	0.036	0.01	1.0×10^{-3}	1.2×10^{-4}	3.0×10^{-3}
C ₂ H	21	8^d	0.16	0.03	3.8×10^{-3}	2.0×10^{-4}	2.0×10^{-3}

a) Based on results listed in Tables 3 and 5; Henning et al. (2010, their Table 3); Thi et al. (2004, their Table 9); and Dutrey et al. (1997, their Table 1 and refs. therein). See §4.

b) R CrA IRS 7B relative abundances from Watanabe et al. (2012, their Table 4, and refs. therein), assuming $N(\text{H}_2)/N(^{13}\text{CO}) = 6 \times 10^5$; IRAS 16293–2422 relative abundances from Schöier et al. (2002, their Table 5).

c) Relative abundances for the planetary nebula (PN) NGC 7027 from Hasegawa & Kwok (2001, their Table 3).

d) Estimated abundance ratio is highly uncertain.